Biosensors and Bioelectronics 221 (2023) 114917

Contents lists available at ScienceDirect

Biosensors and Bioelectronics

journal homepage: www.elsevier.com/locate/bios

Genetically encoded dual fluorophore reporters for graded oxygen-sensing in light microscopy

Nadine Bauer [a], Ivan Maisuls [b,c], Abel Pereira da Graça [a,d], Dirk Reinhardt [a], Raghu Erapaneedi [a], Nils Kirschnick [a], Michael Schäfers [a], Carsten Grashoff [e], Katharina Landfester [f], Dietmar Vestweber [d], Cristian A. Strassert [b,c], Friedemann Kiefer [a,d,*]

[a] European Institute for Molecular Imaging, University of Münster, Röntgenstraße 16, D-48149, Münster, Germany
[b] Institut für Anorganische und Analytische Chemie, University of Münster, Corrensstraße 28-30, D-48149, Münster, Germany
[c] CeNTech, CiMIC, SoN, Heisenbergstraße 11, D-48149, Münster, Germany
[d] Max-Planck-Institute for Molecular Biomedicine, Röntgenstraße 20, D-48149, Münster, Germany
[e] Institute of Integrative Cell Biology and Physiology, University of Münster, Schlossplatz 5, D-48149, Münster, Germany
[f] Max-Planck-Institute for Polymer Research, Ackermannweg 10, D-55128, Mainz, Germany

ARTICLE INFO

Keywords:
Oxygen-sensing
Fluorescent reporter
Ratiometric sensor
FRET-FLIM
Live-cell imaging
Tumor-hypoxia

ABSTRACT

Hypoxia is an essential regulator of cell metabolism, affects cell migration and angiogenesis during development and contributes to a wide range of pathological conditions. Multiple techniques to assess hypoxia through oxygen-imaging have been developed. However, significant limitations include low spatiotemporal resolution, limited tissue penetration of exogenous probes and non-dynamic signals due to irreversible probe-chemistry. First genetically-encoded reporters only partly overcame these limitations as the green and red fluorescent proteins (GFP/RFP) families require molecular oxygen for fluorescence. For the herein presented ratiometric and FRET-FLIM reporters dUnORS and dUnOFLS, we exploited oxygen-dependent maturation in combination with the hypoxia-tolerant fluorescent-protein UnaG. For ratiometric measurements, UnaG was fused to the orange large Stokes Shift protein CyOFP1, allowing excitation with a single light-source, while fusion of UnaG with mOrange2 allowed FRET-FLIM analysis. Imaging live or fixed cultured cells for calibration, we applied both reporters in spheroid and tumor transplantation-models and obtained graded information on oxygen-availability at cellular resolution, establishing these sensors as promising tools for visualizing oxygen-gradients *in-vivo*.

1. Introduction

Oxygen is essential for metazoan life and hypoxia, the disequilibrium of oxygen-consumption and -delivery, has been intensely investigated in development and pathological conditions (Span and Bussink, 2015). Various techniques for the assessment and visualization of hypoxic microenvironments within multicellular systems have been developed (Roussakis et al., 2015). Histomorphometric studies of fixed tissue provided first quantifications of the distance between vessels and hypoxic regions (Thomlinson and Gray, 1955) and initial measurements of local oxygen-concentrations within living tissues were performed using invasive polarographic needles, which are limited by their own oxygen-consumption and tissue compression (Raleigh et al., 1996). Less invasive, quantitative oxygen-imaging is possible using exogenous fluorescent- and/or phosphorescent-(nano)probes (Kiyose et al., 2010; Lecoq et al., 2011; Papkovsky and Dmitriev, 2013), which are however upon *in-vivo* application excluded from the parenchyma of most tissues and require constant perfusion. Non-invasive organ or whole-body imaging is finally achieved by magnetic resonance imaging (MRI) or positron emission tomography (PET) with nitroimidazole-based probes (Nunn et al., 1995; Apte et al., 2011) however, these imaging modalities lack cellular resolution (Roussakis et al., 2015).

In contrast, genetically-encoded reporters based on fluorescent-proteins (FPs) visualize hypoxia directly within each investigated cell, allowing to follow hypoxia and its impact on the cellular microenvironment longitudinally (Takahashi et al., 2006; Papkovsky and Dmitriev, 2018). Ratiometric fluorescence sensors further enable quantitative oxygen-imaging for visualization of local oxygen-concentrations (Lidsky et al., 2018; Misra et al., 2017). However, common FPs of the GFP and RFP-families are poorly suited as

* Corresponding author. European Institute for Molecular Imaging / Multiscale Imaging Center, Röntgenstraße 16, D-48149. Münster, Germany.
E-mail address: fkiefer@uni-muenster.de (F. Kiefer).

https://doi.org/10.1016/j.bios.2022.114917
Received 12 April 2022; Received in revised form 31 October 2022; Accepted 13 November 2022
Available online 17 November 2022

hypoxia-reporters due to slow oxygen-dependent maturation and scaffold-rearrangement, essential for their fluorescence (Remington, 2006; Heim et al., 1994). These limitations were overcome by FPs, which adapt their fluorescent-state oxygen-independently upon binding of endogenously present or exogenously applied fluorogenic cofactors (fluorogens) (Peresse and Gautier, 2019). One example is the green FP UnaG from the Japanese eel, which acquires fluorescence by binding the porphyrin-metabolite bilirubin (BR) (Kumagai et al., 2013), making UnaG ideal for the generation of genetically-encoded hypoxia-sensors. The functionality of UnaG-based hypoxia-sensors, driven by hypoxia-inducible gene expression, was proven *in-vitro* and *in-vivo* (Erapaneedi et al., 2016; Panicucci et al., 2020; Schmitz et al., 2020).

Here, we introduce two novel, genetically-encoded, UnaG-based oxygen-reporters, dUnORS (destabilized-UnaG-CyOFP1-Ratiometric-Sensor) and dUnOFLS (destabilized-UnaG-mOrange2-Fluorescence-Lifetime-Sensor), which were derived from the recently described destabilized-UnaG-mOrange2-Hypoxia-Reoxygenation-Sensor (dUnOHR, Erapaneedi et al., 2016). Both new sensors aim for a graded assessment of tissue oxygen-concentration and their sensing-moiety, like the one of dUnOHR is comprised of a fusion-protein exploiting the dual-emission characteristics and differential oxygen-requirements of oxygen-dependent and -independent FPs.

The UnaG-mOrange2 fusion protein dUnOHR was expressed under a hypoxia-responsive promotor-element (HRE), requiring hypoxia-inducible transcription factor (HIF) binding to HREs and allowing it to mark areas of reoxygenation after transient hypoxia *in-vitro* and *in-vivo* (Erapaneedi et al., 2016). Consequently, in the absence of the cellular HIF-response, dUnOHR expression ceases under normoxia. To overcome this limitation and unlock the potential of a ratiometric analysis, dUnORS and dUnOFLS are expressed under a constitutively active human cytomegalovirus (CMV)-promoter, uncoupling their expression from the cellular response to oxygen-deprivation. To enable faster switching-kinetics of the UnaG-based hypoxia fusion-protein sensors, a turnover enhancing PEST degradation-motif was fused C-terminally to the sensor-constructs (Li et al., 1998; Rogers et al., 1986). As shown by live-cell imaging experiments (Erapaneedi et al., 2016), the PEST-motif decreases the lifetime of UnaG from 20 h to 8 h, while fusion to the HIF1α-derived degradation domain reduced the life time to 5 h and a combination of both even to 30 min. While highly destabilized proteins allow faster switching-kinetics, their overall accumulation and hence brightness is correspondingly reduced. These previous studies indicated that a single C-terminal PEST-domain may provide the optimal compromise between switching kinetics and brightness. Here, we characterize the new sensors dUnORS and dUnOFLS for the detection of molecular oxygen (O_2) *in-vitro,* but also for the visualization of oxygen-gradients within intracranial, *in-vivo* grown glioblastomas.

2. Materials and Methods

A detailed Materials and Methods-section is presented in the Supplementary Information.

2.1. Plasmid design

CMV-dUnORS, contains an UnaG-CyOFP1 expression-cassette with a PEST degradation-sequence expressed from the CMV-promoter. For generation of CMV-dUnOFLS, the HRE-promoter sequence of HRE-dUnOHR was replaced by the CMV-promoter. CMV-UnaG and the maturation-deficient mOrange2-mutant dUnOFLS(G220A) were used as controls. For the latter, a point mutation within mOrange2 generated a non-fluorescent mutant (confirmed by flow cytometry in Suppl. Fig. 1).

2.2. Cell-lines

Cell-bulks stably expressing CMV-dUnORS or CMV-dUnOFLS were derived by selection and fluorescence activated cell sorting (FACS) (Suppl. Fig. 2). For oxygen-depletion experiments, cells were incubated at the indicated ambient oxygen-concentrations.

2.3. Isolation of a cell-free enriched solution of the FRET-reporter

The reporter CMV-dUnOFLS and the respective control dUnOFLS (G220A) were isolated from transiently transfected HEK293T cells via cell lysis and ultracentrifugation. Subsequently, the fluorescence life-times of the cell-free enriched protein solutions were analyzed as described in 2.7. FRET-FLIM.

2.4. Formation of tumor-cell spheroids

Spheroids were grown following a protocol based on liquid-overlay techniques and cell-aggregation methods (Metzger et al., 2011; Maritan et al., 2017; Costa et al., 2014).

2.5. Intracranial tumor-injections

Gli36 reporter cell-lines were intracranially injected into SCID-mice. Tumors were grown for approximately 20 days before intravenous PECAM-1 antibody (Wegmann et al., 2006) injection to contrast blood vessels, followed by euthanization. Brains were explanted, fixed with 3% glyoxal or 4% PFA-fixative and vibratome-sectioned.

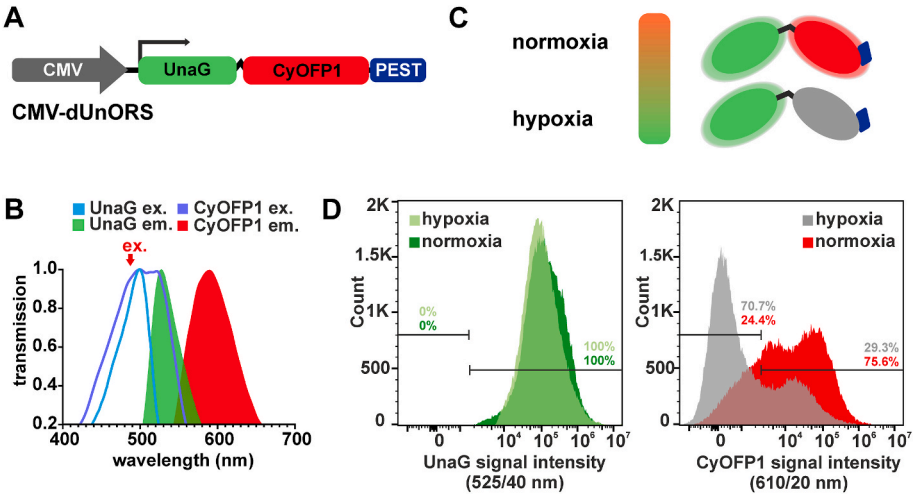

Fig. 1. Properties of the genetically-encoded, ratiometric oxygen-sensor CMV-dUnORS. A) Scheme of CMV-dUnORS. A PEST-motif destabilized UnaG-CyOFP1 fusion-protein, is expressed under control of the human cytomegalovirus (CMV)-promoter. **B)** Excitation (open curves) and emission (filled curves) spectra of UnaG and CyOFP1 (Chu et al., 2016; Kumagai et al., 2013). Due to the LSS of CyOFP1, both FPs are efficiently excited at 470–490 nm (red arrow). **C)** Schematic of dUnORS functionality. UnaG (green) adopts its fluorescence independent of the O_2-availability (reference-signal), whereas fluorescence-maturation of CyOFP1 (red) requires O_2 (sensing-signal). **D)** Cytometric characterization of stably dUnORS-expressing CHO-cell bulks grown under normoxic (18% O_2) or hypoxic conditions (1% O_2) for 40 h. UnaG- (green, 525 nm) and CyOFP1-positive (red, 610 nm) cells were quantified, exhibiting a decrease in CyOFP1-signal intensity under hypoxia.

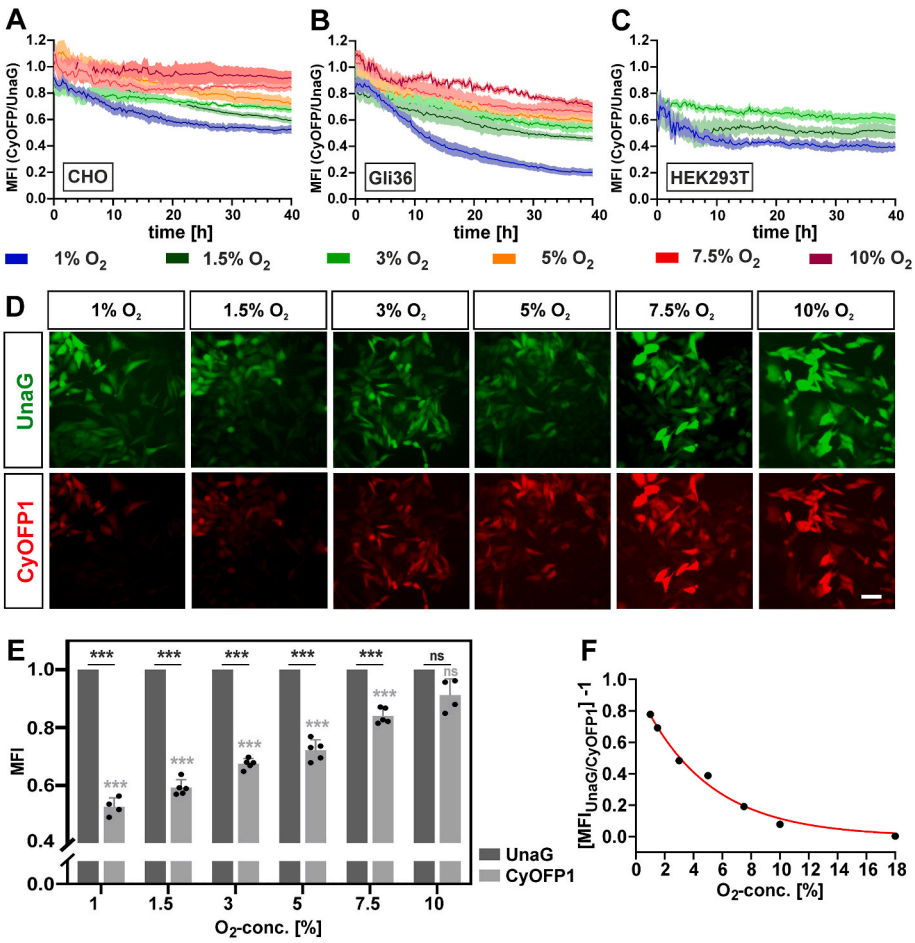

Fig. 2. The CyOFP1/UnaG-fluorescence intensity-ratio in stably dUnORS-expressing cell-bulks correlates with the ambient oxygen-concentration. **A-C**) Temporal change of the CyOFP1/UnaG-MFI ratio in bulk cell cultures (CHO /Gli36 /HEK293T) stably expressing dUnORS. Cells were grown for 24 h at ambient oxygen before being shifted to the indicated oxygen-concentrations (0 h). Fluorescence was recorded every 15 min at 525/50 nm (green) and 645/75 nm (red); excitation at 470 nm. Line graphs depict the mean and s.d. of five viewfields in each series., **D**) UnaG- and CyOFP1-fluorescence in dUnORS-expressing CHO bulk cell culture (40 h time point of timelapse in A), filter-settings a described for A-C). Scale-bar: 100 μm. **E**) Quantification of UnaG- and CyOFP1-MFI depicted in D). Shown are relative fluorescense-intensities normalized to UnaG, bars depict the mean and s.d. of 4 or 5 viewfields. Significance is indicated for the relative difference in the UnaG/CyOFP1-MFI (black asterisks) and the change in CyOFP1-MFI (0 h vs 40 h, gray asterisks). (***$p < 0.001$, ns (not significant) $p \geq 0.05$). **F**) Intensity-ratio [UnaG/CyOFP1]-1 of dUnORS-expressing CHO-cells plotted against the ambient oxygen-concentration.

2.6. Microscopy

A Nikon Ti2-E epifluorescence microscope with an incubation-chamber, enabling dynamic adjustment of oxygen-concentration between 1% and 18%, was used for live-cell time-lapse-imaging of dUnORS. Both FPs were excited at 470 nm and independently visualized via dichroic filter-cubes (525/50 nm, 645/75 nm). For confocal analysis, tumor-cell spheroids and tissue-sections were excited at 488 nm.

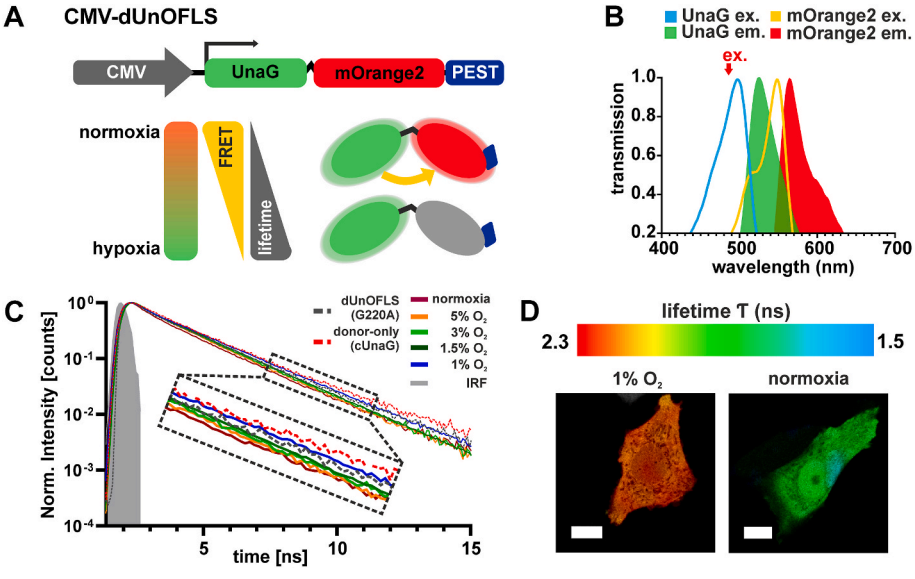

Fig. 3. Structure and *in-vitro* characterization of the fluorescence lifetime-based oxygen-sensor CMV-dUnOFLS

A) Scheme of CMV-dUnOFLS, the destabilized FRET-sensor UnaG-mOrange2(PEST) fusion-protein, and its oxygen-sensing principle. UnaG matures oxygen-independent, whereas mOrange2 requires O_2. FRET (yellow arrow) is strong under normoxia and reduced under hypoxia, resulting in an increasing UnaG-lifetime. **B**) Spectral properties of the UnaG-mOrange2 FRET pair (open curves: excitation; filled curves: emission) demonstrating the overlap between UnaG-emission (donor) and mOrange2-excitation (acceptor) (Kumagai et al., 2013; Shaner et al., 2008). **C)** Photon-count histogram of UnaG-lifetime measurements in dUnOFLS-expressing CHO-cells. Decay-curves exhibit a shift of the photon-count plot, corresponding to a gradual increase in the UnaG-lifetimes ($\tau_{Av.Amp.}$) under progressive oxygen-depletion, approaching the donor-only lifetimes (τ_D) of cUnaG or the dUnOFLS(G220A) mutant. IRF: instrument response function. **D**) Lifetime-images of dUnOFLS-expressing CHO-cells grown at 1% or ambient oxygen, depicting the UnaG-lifetime ($\tau_{Av.Amp.}$) after pulsed laser excitation at 485 nm and the corresponding LUT of the photon-count-lifetime conversion. Scale-bars: 10 μm.

2.7. FRET-FLIM

A FLIM detection unit (PMA Hybrid Series, PicoQuant, Berlin, GER) coupled to an LSM 880 (Zeiss) confocal microscope equipped with a 63x oil immersion objective (Zeiss 63× Plan Apo, NA = 1.4) was used for TCSPC-FLIM analysis of living cells expressing the FRET-sensor dUnOFLS. For live-cell imaging at various oxygen concentrations a microscope temperature- and gas-control system was used (Life Imaging Services, Basel, CHE). After pulsed laser excitation at 485 nm (PDL 828, PicoQuant), UnaG-lifetime was measured at 520/35 nm to block acceptor-photons and analyzed by SymPhoTime64 software (PicoQuant). For FRET-FLIM analysis, first, the mean UnaG-only lifetimes ($\overline{\tau_D}$) were measured in the absence of, or in the presence of a maturation-deficient acceptor-fluorophore (donor-only construct cUnaG or mutated sensor construct mOrange2(G220A)) and fitted by a monoexponential decay model. Analysis of the amplitude-weighted UnaG-lifetime in the presence of its acceptor ($\tau_{Av.Amp.}$) in dUnOFLS was performed keeping $\overline{\tau_D}$ of the G220A-mutant-construct as a fixed variable while applying a biexponential fitting model (Sillen and Engelborghs, 1998; Peter et al., 2005). The fitting-constrain implied by the fixation of the $\overline{\tau_D}$-variable is justified by the oxygen-independence of the UnaG-only lifetime (Suppl. Fig. 3), validating UnaG as reference-signal. The applied computation relies on the multi-exponential tailfit-model of the SymphoTime64 software, whereas $\tau_{Av.Amp.}$ is defined according to the following equation (1):

$$\tau_{Av.Amp.} = \frac{\sum_i Ampl_i \times \tau_i}{\sum_i Ampl_i} \quad (1)$$

The goodness-of-fit was evaluated by considering the χ^2-distribution during each calculation of $\tau_{Av.Amp.}$. For lifetime-measurements of dUnOFLS expressing tumor spheroids and fixed vibratome sections of intracranial tumors, the same settings of the FLIM-unit were applied, utilizing 10x (Zeiss Plan Apo, NA = 0.45) and 40x (Zeiss C Apo, NA = 1.2) objectives.

2.8. Two-photon-FLIM

Two-Photon excited lifetime measurements on fixed cells and tissue samples were performed using an IX 73 confocal microscope (Olympus, Hamburg, GER) coupled to a laser combining unit and a multichannel detection unit (Microtime 200, PicoQuant). A two-photon Ti:Sapphire (Ti:Sa) Mai Tai® Ultrafast Laser (MSK | Spectra Physics, Stahnsdorf, GER), with a tuning range of 690–1040 nm, was equipped to the main optical unit (MOU) and used as the excitation source at 810 nm, making sure to exclusively excite the donor-fluorophore (Suppl. Fig. 4). The Ti:Sa Laser was connected to a Pulse Picker (A.P.E.®, Berlin, GER) while the scanning was performed using the Galvo Scanner FLIMbee (PicoQuant). For signal detection a Hybrid-Photomultiplier detector was used, whereas the data acquisition was based on the method of TCSPC. Band pass and/or low pass filters were used accordingly, depending on the desired experiment as well as the wavelength of the excitation source. Lifetime-analysis was performed as outlined in 2.7., applying the same fitting models.

2.9. Image and data analysis

Image analysis was performed using FIJI by ImageJ (Schindelin et al., 2012). A custom ImageJ-plugin enabled automated processing of the time-lapse-image series (Suppl. Fig. 5+6). Statistical analysis and sample numbers are indicated in the figure-legends and dUnORS signal-intensities were determined following the Holm-Šídák-method; dUnOFLS FLIM-data were analyzed by the Kolmogorov-Smirnov-test and calculations performed using Excel or GraphPad-PRISM. Corresponding significances are represented by the p-value (NJEM-formatting): ***p < 0.001, **p = 0.001–0.01, *p = 0.01–0.05, ns (not significant) p ≥ 0.05. The Stern-Volmer-constant K_{SV} was calculated according to the slope-value of the corresponding regression-line.

3. Results

3.1. CMV-dUnORS: reporter for ratiometric oxygen-sensing

In CMV-dUnORS the UnaG-CyOFP1 fusion-protein is constitutively expressed under control of the human cytomegalovirus(CMV)-promoter (Fig. 1A) and mOrange2 of dUnOHR was replaced by the orange large Stokes Shift (LSS) FP CyOFP1 (Chu et al., 2016), enabling simultaneous excitation of both proteins (Fig. 1B, red arrow). This avoids intensity ratio fluctuations between the two light-sources, which are required for the excitation of dUnOHR, impairing its suitability for ratiometric

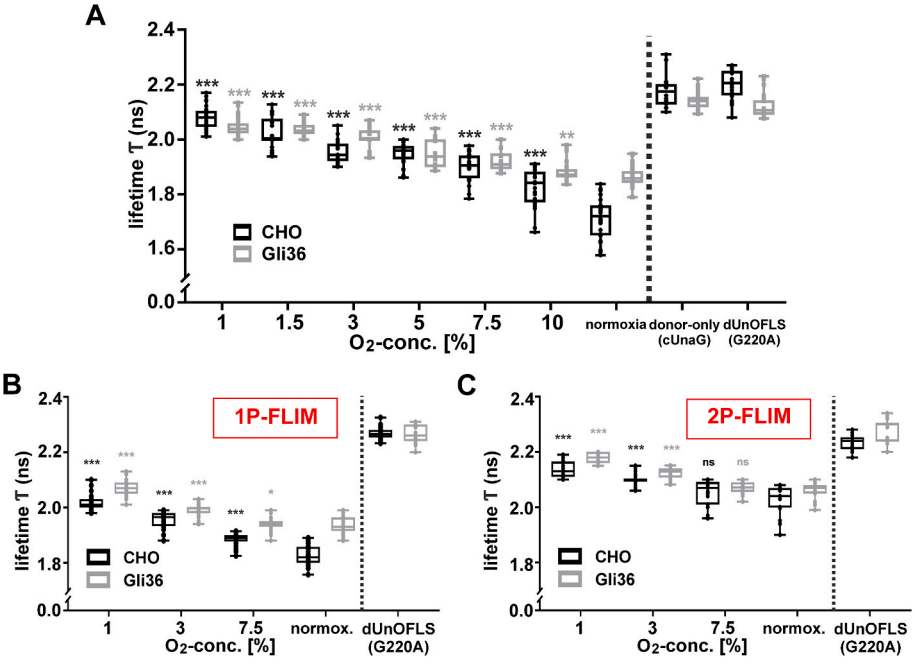

Fig. 4. Graded sensing of ambient O_2 using dUnOFLS lifetime-measurement in living and PFA-fixed cells. Statistical significance was determined for the change in the UnaG-lifetime in CHO- and Gli36-cells expressing dUnOFLS under oxygen-depletion compared to lifetimes at normoxia. **A)** Cells were cultured for 30 h at the indicated oxygen-concentrations and calculated average lifetimes of UnaG ($\tau_{Av.Amp.}$) were determined in a live-cell experiment. Control-lifetimes were measured in cells expressing cUnaG or dUnOFLS(G220A). The latter formed the basis for determination of $\tau_{Av.Amp.}$ within dUnOFLS ($\overline{\tau_D}$: 2.18 (CHO) and 2.13 ns (Gli36)). (***p < 0.001 and **p = 0.001–0.01; Mean ± SD; n = 21–60) **B)** Cells were cultured at the indicated oxygen-concentrations for at least 20 h, fixed in 4% PFA/PBS and UnaG-lifetimes ($\tau_{Av.Amp.}$) were determined as described in A). $\overline{\tau_D}$ of dUnOFLS(G220)**:** 2.2 ns (CHO) and 2.25 ns (Gli36). (***p < 0.001, *p = 0.01–0.05; Mean ± SD; n = 29–43) **C)** CHO- and Gli36-cells were cultured as described in C), the UnaG-lifetimes of dUnOFLS(G220A) ($\overline{\tau_D}$: 2.2 ns (CHO) and 2.25 ns (Gli36)) determined and used for the dUnOFLS-lifetime ($\tau_{Av.Amp.}$) analysis following 2P-excitation. (***p < 0.001, ns (not significant) p ≥ 0.05; Mean ± SD; n = 21–29).

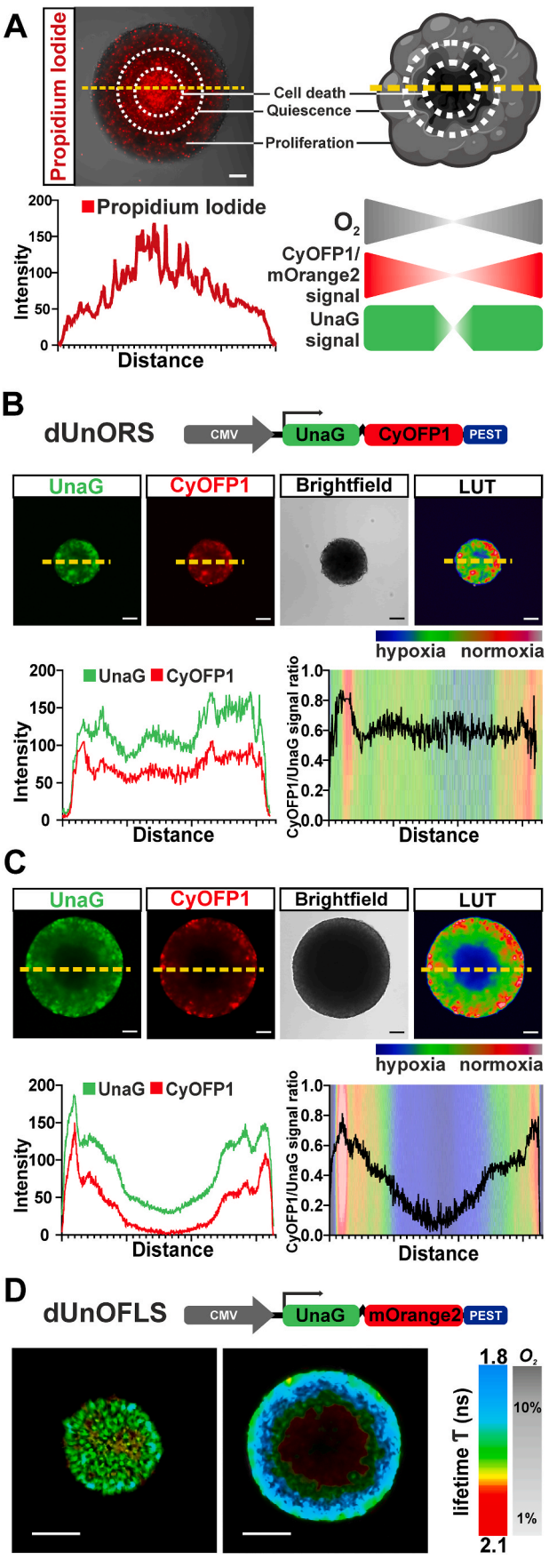

(caption on next column)

Fig. 5. Graded response of dUnORS and dUnOFLS in a 3D-tumor-spheroid model. A) Left: Confocal section through the central plane of a propidium iodide (PI)-stained Gli36 tumor-spheroid and corresponding fluorescence-intensity plot, indicating necrotic core formation. Right: CyOFP1-/mOrange2-fluorescence is expected to decrease from the peripheral (proliferative and quiescent) zones towards the centre due to restricted oxygen-diffusion and necrotic core formation. Scale-bar: 100 μm. **B + C)** Top: Confocal equatorial section through dUnORS-expressing Gli36-cell tumor-spheroids. Shown are the UnaG, CyOFP1 and brightfield signals and a projection of the CyOFP1/UnaG-ratio. Bottom: Fluorescence-intensity and CyOFP1/UnaG-fluorescence ratio plots across the spheroid diameter (position corresponding to the yellow line in the confocal sections). Scale-bars: 100 μm. **D)** UnaG-lifetimes ($\tau_{Av.Amp.}$) in the central focal plane of spheroids formed by dUnOFLS-expressing Gli36-cells. The lifetime-LUT was derived from the values determined in Fig. 4A. Scale-bars: 200 μm.

measurements. CyOFP1 is comparably bright to mOrange2, but matures significantly faster (CyOFP1: 15 min, mOrange2: 2.5 h) (Chu et al., 2016; Shaner et al., 2008), which combined with the degradation PEST-motif improves the dynamic response of dUnORS, enabling faster sensor-adjustment to variations in the ambient oxygen-concentrations (Li et al., 1998; Rogers et al., 1986). Here, CyOFP1-emission provided the oxygen-sensing signal, whereas UnaG acted as the oxygen-independent internal reference (Fig. 1C, Suppl. Fig. 7). To demonstrate the sensor-functionality, analysis was performed with FACS-sorted bulk cell cultures (CHO /Gli36 /HEK293T) expressing intermediate to high dUnORS-levels, aiming to average clonal variation-effects and avoid potential toxicity of excessive FP expression (Suppl. Fig. 2). Cytometry of UnaG- and CyOFP1-fluorescence in CHO-cultures prior and following incubation under oxygen-depletion (1% O_2) revealed a strong oxygen-dependence of the CyOFP1-signal (Fig. 1D), while stable UnaG-fluorescence was detected independent of the ambient oxygen-concentration.

3.2. Oxygen-dependency of CyOFP1-maturation in dUnORS enables ratiometric oxygen-sensing

Having verified a strong oxygen-limited restriction of CyOFP1-maturation, we determined if the CyOFP1/UnaG-fluorescence ratio correlated with the ambient oxygen-concentrations. Thus, cell-bulks (CHO /Gli36 /HEK293T) were grown for 40 h at the conditions indicated in Fig. 2. UnaG- and CyOFP1-fluorescence were recorded every 15 min using an epifluorescence microscope. The mean fluorescence intensities (MFIs) of both channels stabilized during the 40 h incubation-period, allowing a ratiometric evaluation (Fig. 2A–C). dUnORS distinguished concentrations between 1 and 10% ambient oxygen in CHO- and Gli36-cells (Fig. 2A + B), while only concentrations between 1 and 3% oxygen were discernible in HEK293T-cells (Fig. 2C). Fig. 2D depicts the 40 h-time point of dUnORS-expressing CHO-bulks, indicating a graded restriction of the CyOFP1-signal under oxygen-depletion. Determination of the corresponding CyOFP1/UnaG-fluorescence ratio displayed the expected corresponding reduction (Fig. 2E). A plot of the ratio [UnaG/CyOFP1]-1 versus the oxygen-concentration, displayed a steep decline between 1 and 10%, but only little change between 10 and 18% oxygen, suggesting the optimal sensor operation-range below and saturation above 10% oxygen (Fig. 2F).

3.3. CMV-dUnOFLS: FRET allows oxygen-sensing in the lifetime-domain

Spectral properties of UnaG and mOrange2 indicate a substantial overlap of UnaG-emission and mOrange2-absorption spectra, suggesting efficient Förster resonance energy transfer (FRET) between the proteins (Fig. 3A + B). To exploit this property for oxygen-sensing, we replaced the HRE-dependent promoter of dUnOHR (Erapaneedi et al., 2016) against a constitutive CMV-promoter, generating dUnOFLS (Fig. 3A). Non-radiative energy transfer between a donor- and an

acceptor-molecule during FRET results in a decrease of the donor fluorescence-lifetime (Förster, 1946; Lakowicz, 1999). Due to the restricted mOrange2-maturation under oxygen-depletion and the insensitivity of the UnaG-lifetime to fluctuations in the oxygen-availability (Suppl. Fig. 3, Suppl. Fig. 7), we expected FRET between UnaG (donor) and mOrange2 (acceptor) to decrease under hypoxia, resulting in increasing UnaG-lifetimes (Fig. 3A). For assessment of FRET, fluorescence lifetime imaging microscopy (FLIM) provides a robust analysis-mode. We decided to measure the UnaG fluorescence-lifetime in the time-domain using time-correlated single--photon counting (TCSPC). We therefore cultured dUnOFLS-expressing CHO-cells at various oxygen-concentrations and measured the decay profiles of the TCSPC-curves, displaying a shift in photon-counts under hypoxia (Fig. 3C). As control-constructs, we used a cUnaG donor-only construct or UnaG fused to the maturation incompetent mOrange2 (G220A)-mutant (Suppl. Fig. 1). The latter allowed determination of the UnaG-lifetime in the context of the UnaG-mOrange2-fusion-protein in absence of FRET due to the non-fluorescent mOrange2(G220A). Under pronounced hypoxia the dUnOFLS photon-count profile approached the decay-curves characteristic for the control-constructs. Intracellular UnaG-lifetimes in the control cell-lines approximated the reported lifetime of 2.21 ns for purified UnaG-protein (Cao et al., 2019). Using the previously defined, averaged lifetime of our control-constructs as reference, we defined a dUnOFLS-specific look-up table (LUT), with amplitude-weighted averaged UnaG-lifetimes ($\tau_{Av.Amp.}$) of approximately 2.2 ns at maximal hypoxia (1% O_2) and approximately 1.6 ns at normoxia (Fig. 3D).

Furthermore, sensor lifetime at normoxic conditions was confirmed by measuring the UnaG-lifetime within dUnOFLS in a cell-free solution obtained from transiently transfected HEK293T cells (Suppl. Fig. 8). To explore the correlation between fluorescence-lifetime and ambient oxygen-concentration, dUnOFLS-expressing CHO- and Gli36-cells were analyzed in live-cell experiments. Both cell-lines displayed the longest UnaG-lifetime under hypoxia (1% O_2), approximating the lifetime of isolated UnaG or UnaG in the context of the maturation-incompetent sensor dUnOFLS(G220A) (Fig. 4A). As expected increasing oxygen-concentrations resulted in a decrease in UnaG-lifetime.

Read-out of dUnOFLS in a tissue context will inevitably rely on post mortem analysis. Therefore, dUnOFLS-expressing cell-monolayers were also analyzed after PFA-fixation and comparatively measured by confocal one (1P)- and two photon (2P)-microscopy (Fig. 4B + C). The fixation process did not have a significant impact, as lifetimes of live and fixed cells were within the same range (Fig. 4B) and were also not altered when determined after increasing intervals following fixation (Suppl. Fig. 9). Analysis by 2P-pulsed laser excitation (810 nm) revealed a small increase in UnaG-lifetime compared to 1P-FLIM (Fig. 4C), importantly, the lifetime-change between cells cultured in 1% oxygen and normoxia showed the same shift as for 1P-excitation (Fig. 4B + C). Furthermore, we assessed, whether the increase in UnaG-lifetime between 1P- and 2P-measurements was caused by the excitation-regime or if it was due to the different microscopic instruments applied. Therefore, a 1P-excited (440 nm) analysis of dUnOFLS-expressing cells was performed using the microscope, filters and detectors used for the multiphoton-experiment. Detected 1P-lifetimes (440 nm excitation) were comparable to the lifetime-measures during the initial 1P-excited (485 nm) FLIM analysis (Suppl. Fig. 10). Hence, instrument-related lifetime differences were minimal in the same excitation-regime. Exciting mOrange2-expressing CHO cells at 810 nm, we noted a complete lack of fluorescence, excluding cross-excitation of mOrange2 as a potential source compromising 2P-FLIM measurements (Suppl. Fig. 4).

3.4. Visualization of oxygen-gradients in a 3D-tumor-spheroid model

To test our sensors in the context of an *in-vitro* 3D-model, we turned to tumor-spheroids, which are widely applied as a simplistic tumor model. During their initial growth, small spheroids are expected to consist mostly of proliferating cells, whereas further growth leads to the development of a quiescent and ultimately necrotic core due to a lack of O_2 (Mueller-Klieser et al., 1986; Freyer and Sutherland, 1986). We grew Gli36-cells into tumor-spheroids of approximately 700 μm diameter and readily detected a core that was stained by propidium iodide (Fig. 5A), confirming previous studies that had demonstrated formation of necrotic cores in spheroids larger than 500 μm (Brüningk et al., 2020; Däster et al., 2017; Khaitan et al., 2006). Using a single excitation wavelength of 488 nm, dUnORS signal-intensities within the central plane of the spheroids were recorded by confocal microscopy. In a small spheroid the CyOFP1/UnaG-fluorescence ratios indicated largely sufficient oxygenation (Fig. 5B), however, in large tumor-spheroids, the complete absence of CyOFP1 and the strong reduction of UnaG-fluorescence were not only indicative of strong hypoxia, but very likely also the result of spheroid-core necrosis (Fig. 5C). Outside this core-area towards the spheroid surface, we measured, based on our previous calibration, ratios corresponding to oxygen-concentrations from 1 to 10% oxygen (Fig. 2B). In addition, tumor-spheroids expressing dUnOFLS (Fig. 5D) reported the presence of an oxygen-gradient within large spheroids, with UnaG-lifetimes roughly corresponding to 1–10% ambient oxygen, as calibrated in the monolayer-experiments (Fig. 4A). Photon-counts dropped sharply towards the spheroid center, which is in agreement with the necrotic core formation detected by propidium iodide staining.

3.5. Approaches towards graded oxygen-sensing in-vivo

For a sensor-analysis in the context of intact organs, the Gli36 reporter cell-lines were intracranially transplanted into mice and vibratome-sections of explanted tumors were analyzed. Fig. 6A depicts a dUnORS-expressing tumor and particularly striking was the predominant UnaG-signal within the tumor-core. The contrasted vasculature (PECAM-1) revealed the irregular, tumor-typical vascular bed, with varying microvessel diameters, indicative of dysfunctionality and poor perfusion. In agreement with an insufficient oxygen-supply, elevated CyOFP1-fluorescence was restricted to the proximity of presumably perfused, larger vessels, whereas UnaG was readily detected at greater distances from these vessels (Fig. 6A, Suppl. Fig. 11A). Visualization of intra-tumoral dUnORS/UnaG fluorescence-ratios via the described LUT indicated a highly heterogeneous hypoxia-landscape.

We repeated the analysis of intracranial tumors now formed by dUnOFLS-expressing Gli36-cells, which also showed distinct differences between densely vascularized areas at the tumor-rim and the scarcely vascularized tumor-core. In accordance, 1P-FLIM revealed a reduced UnaG-lifetime in the tumor periphery, where maturation of mOrange2 is inferred as well as prolonged lifetimes in the tumor-core, indicating hypoxia and predominantly UnaG-derived signals (Fig. 6B – close-up views).

Intravital microscopy benefits strongly from the increased tissue-penetration achieved by near-infrared excitation in multiphoton-microscopy. To explore a possible application of dUnOFLS in intravital analysis, we compared sections of dUnOFLS-expressing intracranial tumors using 1P- and 2P-FLIM (Fig. 6C + D). The tumor visualized in the top-panel showed decreased lifetimes corresponding to a moderately oxygenated region in the tumor-center, colocalizing with several large blood vessels. This central area was flanked by regions with predominantly longer UnaG-lifetimes and a comparatively low vessel density (Fig. 6C – close-up view). In the glioma shown in the bottom-panel, the formation of ring-shaped zones with increased UnaG-lifetime around selected large vessels was remarkable (Fig. 6C). Close-up views revealed a small rim of well-oxygenated cells proximal to the vessels, surrounded by a larger ring of increasingly hypoxic tumor-cells up to a distance of 100 μm (Fig. 6C – close-up). 2P-FLIM visualizations of corresponding regions (Fig. 6D) up to cellular resolution (Suppl. Fig. 11B) revealed consistently comparable patterns of the intra-tumoral oxygen-landscape.

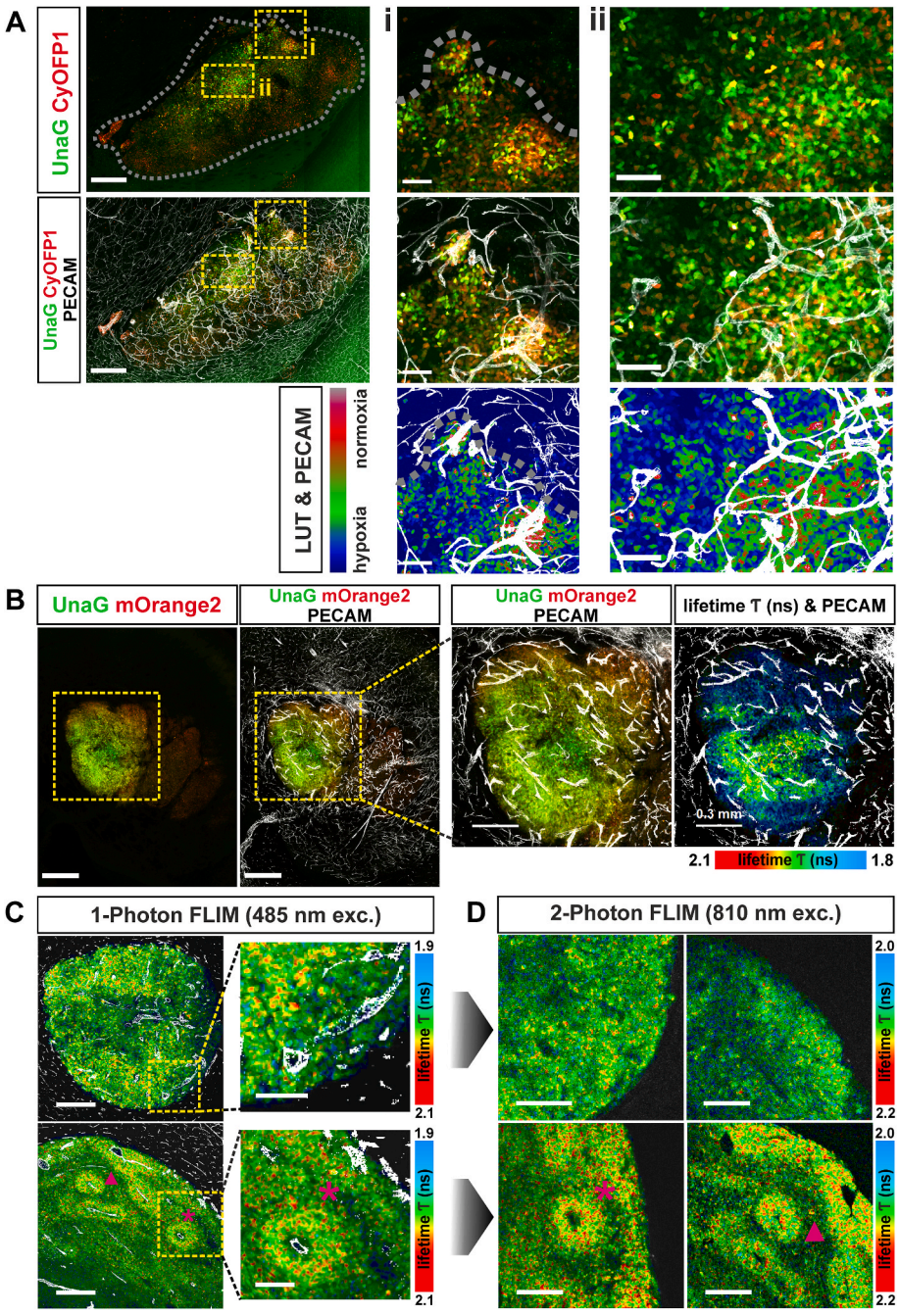

Fig. 6. Intracranial tumors formed by UnaG-oxygen-sensor expressing cells. Stably dUORS- or dUnOFLS-expressing human glioma-cells (Gli36) were orthotopically injected into mice. Shown are vibratome brain-sections of explanted organs. Visualized is the endogenous sensors-fluorescence or corresponding UnaG-lifetimes, while vasculature was stained by intravenous injection of labelled PECAM-1-antibodies (white). **A)** Overview of dUnORS-expressing tumors revealing a heterogeneous CyOFP1/UnaG-signal ratio. A scarcely vascularized central tumor-area (ii) shows low signal-ratio, while densely vascularized areas (i) display higher signal-ratios. Scale-bars: 500 μm (overview), 100 μm (close-up view). Bottom: LUT visualization of CyOFP1/UnaG-ratio, PECAM1 delineates vasculature. **B)** Overview of dUnOFLS-expressing tumor with spatial variation of the UnaG-lifetime ($\tau_{Av.Amp.}$) determined by 1P-microscopy. Close-up views of the intra-tumoral volume revealed increased UnaG-lifetimes after 485 nm-excitation, in particular towards the tumor-core. Scale-bars: 500 μm (overview), 300 μm (close-up view). **C + D)** dUnOFLS-expressing tumors, analyzed by 1P-(485 nm) and 2P-(810 nm) excited FLIM (identical instrument). Both modalities revealed similar UnaG-lifetime ($\tau_{Av.Amp.}$) distribution patterns. Purple arrowheads and asterisks indicate corresponding structures within both microscopic modalities. Scale-bars: 300 μm (1P-overview), 100 μm (1P-close-up view), 200 μm (2P-overview).

4. Discussion

Despite the central role of hypoxia during development and disease, there is still a lack of methodology to visualize O_2-availability longitudinally and with cellular resolution in entire organs or organisms. Here, we report two novel genetically encoded hypoxia-sensors: dUnORS and dUnOFLS, in which the oxygen-independent FP UnaG provides the reference-signal, while the oxygen-dependent FPs CyOFP1 and mOrange2 act as sensing-units. Thus, the equimolar presence of both sensor and reference within the fusion-proteins allowed a straightforward ratiometric (dUnORS) or fluorescence lifetime-based (dUnOFLS) readout. We calibrated both sensors using stable cell-lines and probed their suitability in *in-vitro* spheroid-models and in an *in-vivo* tumor transplantation-model. Both sensors indicated the presence of oxygen-gradients under circumstances where these had been reported previously, supporting for their functionality and applicability. dUnORS can be readily used on any fluorescence microscope, however, fluorescence ratios will depend on the actual filter-sets used. dUnOFLS requires a more complex setup, which however is less susceptible to inter-instrument variations (Fig. 4 + 6) due to determination of the physical observable fluorescence-lifetime. Application of this FLIM sensor in live cell and intravital microscopy is only limited by the requirement for collection of sufficient photons without inducing toxic effect due to forced protein expression or phototoxicity. We do not refer to our approach as quantitative measurement because we do not report absolute tissue oxygen concentrations. However, we attribute individual cells relative oxygen-levels with reference to cultured cells grown at specific ambient O_2-concentrations; here, referred to as graded oxygen imaging.

Previously, FRET has been used to visualize hypoxia-mediated acti-

vation of the HIF1-pathway after nuclear HIF1α/1β-heterodimer formation (Prost-Fingerle et al., 2017). Combination of reference (donor)- and sensing (acceptor)-moieties within one molecule provides a robust read-out, is independent of the sensor-concentration and well-established for FRET-biosensors (Bolbat and Schultz, 2017). One FRET-based hypoxia sensor exploited the affinity of the HIF1α-derived oxygen-dependent degradation domain and the Hippel-Lindau tumor suppressor (VHL) to juxtapose the ECFP and YPet in normoxia (Youssef et al., 2016). Different to the use of FRET as a molecular ruler, dUnOFLS senses the environmental parameter O_2 via mOrange2-maturation. Changes in the UnaG-lifetimes ($\tau_{Av.Amp.}$) therefore reflect the number of oxygen-independent UnaG-molecules capable of energy transfer to the, under hypoxic conditions maturation-deficient mOrange2, best approximated with a biexponential-fit (Sillen and Engelborghs, 1998). The oxygen-dependence of aquatic FPs was already exploited in the FRET-pair of oxygen-sensitive yellow-FP (YFP) and oxygen-tolerant flavin-binding-FP (FbFP) for O_2-sensing in bacteria (Potzkei et al., 2012). However, the functionality of the FbFP-based sensor might be limited in higher eukaryotes due to the lack of the *de-novo* riboflavin-machinery (Merrill et al., 1981) and a sensor-analysis within mammalian cells has not been published. Like FbFP, UnaG matures oxygen-independent, but utilizes unconjugated BR as its fluorophore (Kumagai et al., 2013), identifying BR-availability as a potentially confounding element in UnaG-based reporters. BR is an open, poorly water-soluble tetrapyrrole, that readily passes the cell membrane and is transported in blood after non-covalent binding to albumin (Nogales and Lightner, 1995). We previously found approximately 3.5 μM unconjugated BR in our tissue culture media (Erapaneedi et al., 2016), providing sufficient BR-supply for sensor-functionality. In this study we detected differences in the intracellular bilirubin concentration of the employed cell lines, which however did not correlate with the detected differences in ratiometric readout (Fig. 2 A-C, Suppl. Table 1).

In contrast to several other sensors (Erapaneedi et al., 2016; Prost--Fingerle et al., 2017; Panicucci et al., 2020; Schmitz et al., 2020, 2021; Youssef et al., 2016), transcription of dUnORS and dUnOFLS was no longer coupled to the cellular hypoxia-response, but constitutively expressed. Although reporter-proteins under control of hypoxia-inducible promotor-elements mostly provide a faithful approach to indicate hypoxia, several potentially confounding non-hypoxic activators of the HIF-pathway have been defined (Dery et al., 2005), and variable promotor-activity or sensor failure bear in this setting the risk of misinterpretation as normoxia.

We characterized dUnORS and dUnOFLS at ambient oxygen-concentrations, ranging from 1% to atmospheric oxygen-levels, defining their working-range within the physiologically relevant O_2-levels of 1–10%. Most mammalian tissues prevail at 2–9% oxygen with tissue-hypoxia occurring at oxygen-levels below 2% and severe hypoxia/anoxia being defined below 0.02% oxygen (Bertout et al., 2008; Ortiz-Prado et al., 2019). Hypoxia-sensors previously described in *Drosophila* defined working-ranges of 5–60% oxygen, thus, acting outside the optimal window of mammalian tissue-oxygenation (Misra et al., 2017; Lidsky et al., 2018). Furthermore, these sensors require prolonged maturation-times of up to 3 days, severely limiting their dynamic response (Lidsky et al., 2018), while dUnORS equilibrated after approximately 24 h of oxygen-depletion (Fig. 2). Further destabilization of the fusion-protein to increase turn-over would improve the dynamic response rate, however, at the cost of lower steady-state protein-levels and hence reduced signal-to-noise ratios. Future attempts to improve the dynamic range of dUnOFLS could include spacer-modifications to optimize the spatial orientation and/or flexibility between donor- and acceptor-fluorochromes, further enhancing FRET-efficiency (Nagai et al., 2004).

Here, we successfully visualized a graded oxygen-distribution in 3D-spheroids *in-vitro* and in *ex-vivo* tissue-slices, derived from intracranially transplanted tumors. As previously observed at the single-cell level, UnaG-based sensor-signals are strongly heterogeneous in hypoxic areas (Erapaneedi et al., 2016; Schmitz et al., 2020). Although BR-production and -availability are subject to physiological changes (Wu et al., 2019), these are unlikely to be responsible for this effect. The heterogeneity may reflect differences in the individual metabolic states of single-cells within a given tissue-volume or be caused by cell-migration towards a more favorable metabolic environment. Within solid glioblastomas, a diversity of metabolic microenvironments has been demonstrated, effecting intra-tumoral gradients of not only oxygen- and nutrient-supply but also oxidative phosphorylation, anabolic metabolism and mTOR-activity, depending on the grade of vascularization (Kumar et al., 2019). In agreement with this report, we noted ring-shaped zones of reduced oxygen-availability, or increased metabolic activity, around selected vessels in many tumor-sections. These blood vessels may be dysfunctional and poorly perfused, a characteristic for intra-tumoral vasculature and emphasizing the importance of large-volume imaging in the analysis of tumor vascularization and microenvironment using endogenous reporter-systems.

5. Conclusions

So far, analysis of hypoxia with cellular resolution was dominated by antibody-mediated detection of neoepitopes, which precluded a live-cell dynamic assessment. Analyzing hypoxia in living organisms is presently best achieved by injection of probes, including phosphorescent-nanoparticles or fluorescent quantum-dots, into selected cavities (Shamirian et al., 2016; Wu et al., 2009; Yoshihara et al., 2012). However, expression of genetically-encoded sensors has been demonstrated to detect hypoxia with cellular resolution independent of perfusion and/or penetration. Here, we characterized two genetically-encoded sensors, dUnORS and dUnOFLS, that allow a graded measurement of tissue oxygen-levels. Hypoxia and even anoxia contribute to a multitude of developmental processes and pathologies including tumor-biology, myocardial infarction, stroke, severe anemia and diabetes, making further *in-vivo* characterizations of our sensors worthwhile. Therefore, the application of these UnaG-based sensors should enable a novel approach to central biomedical questions by future intravital (multi-photon) light-microscopic studies.

Authors contributions

FK and NB designed and evaluated experiments and wrote the manuscript. NB generated reagents and performed experiments. IM provided support with 2P-FLIM-measurements and DR executed intracranial tumor-injections, CG provided support with FLIM-analysis, APG, RE, CAS, DV, KL, NK and MS provided reagents and contributed conceptually.

Declaration of competing interest

The authors declare that they have no known competing financial interests or personal relationships that could have appeared to influence the work reported in this paper.

Data availability

Data will be made available on request.

Acknowledgements

We thank Martin Stehling (Flow Cytometry-Unit of the Max-Planck-Institute Münster) for expert technical support and Thomas Huser for inspiring discussions. We thank Steffen Rüttinger, PicoQuant for support and helpful discussion on FLIM evaluation. We gratefully acknowledge funding by the Deutsche Forschungsgemeinschaft to FK, DV, KL, MS (SFB1450/1–431460824) and to CAS (SFB1450/1–431460824; EXC1003-194347757) and by Studienstiftung des Deutschen Volkes to

NB. IM gratefully acknowledges the Alexander-von-Humboldt-Stiftung for support. We acknowledge support from the Open Access Publication Fund of the University of Muenster.

Appendix A. Supplementary data

Supplementary data to this article can be found online at https://doi.org/10.1016/j.bios.2022.114917.

References

Apte, S., Chin, F.T., Graves, E.E., 2011. Curr. Org. Synth. 8, 593–603.
Bertout, J.A., Patel, S.A., Simon, M.C., 2008. Nat. Rev. Cancer 8, 967–975.
Bolbat, A., Schultz, C., 2017. Biol. Cell. 109, 1–23.
Brüningk, S.C., Rivens, I., Box, C., Oelfke, U., Ter-Haar, G., 2020. Sci. Rep. 10, 1–13.
Cao, X., Zhang, C., Gao, Z., Liu, Y., Zhao, Y., Yang, Y., Chen, J., Jimenez, R., Xu, J., 2019. Phys. Chem. Chem. Phys. 21, 2365–2371.
Chu, J., Oh, Y., Sens, A., Ataie, N., Dana, H., Macklin, J.J., Laviv, T., Welf, E.S., Dean, K. M., Zhang, F., Kim, B.B., Tang, C.T., Hu, M., Baird, M.A., Davidson, M.W., Kay, M.A., Fiolka, R., Yasuda, R., Kim, D.S., Ng, H.-L., Lin, M.Z., 2016. Nat. Biotechnol. 34 (7), 760–767.
Costa, E.C., Gaspar, V.M., Coutinho, P., Correia, I.J., 2014. Biotechnol. Bioeng. 111 (8), 1672–1685.
Däster, S., Amatruda, N., Calabrese, D., Ivanek, R., Turrini, E., Droeser, R.A., Zajac, P., Fimognari, C., Spagnoli, G.C., Iezzi, G., Mele, V., Muraro, M.G., 2017. Oncotarget 8 (1), 1725–1736.
Dery, M.A., Michaud, M.D., Richard, D.E., 2005. IntJBiochemCellBiol 37, 535–540.
Erapaneedi, R., Belousov, V.V., Schäfers, M., Kiefer, F., 2016. EMBO J. 35, 102–113.
Förster, T., 1946. Naturwissenschaften 33, 166–175.
Freyer, J.P., Sutherland, R.M., 1986. Cancer Res. 46 (7), 3504–3512.
Heim, R., Prasher, D.C., Tsien, R.Y., 1994. Proc. Natl. Acad. Sci. U.S.A. 91 (26), 12501–12504.
Khaitan, D., Chandna, S., Arya, M.B., Dwarakanath, B.S., 2006. J. Transl. Med. 4, 1–13.
Kiyose, K., Hanaoka, K., Oushiki, D., Nakamura, T., Kajimura, M., Suematsu, M., Nishimatsu, H., Yamane, T., Terai, T., Hirata, Y., Nagano, T., 2010. J. Am. Chem. Soc. 132 (45), 15846–15848.
Kumagai, A., Ando, R., Miyatake, H., Greimel, P., Kobayashi, T., Hirabayashi, Y., Shimogori, T., Miyawaki, A., 2013. Cell 153, 1602–1611.
Kumar, S., Sharife, H., Kreisel, T., Mogilevsky, M., Bar-Lev, L., Grunewald, M., Aizenshtein, E., Karni, R., Paldor, I., Shlomi, T., Keshet, E., 2019. Cell Metabol. 30 (1), 201–211.
Lakowicz, J.R., 1999. Principles of Fluorescence Spectroscopy. Springer.
Lecoq, J., Parpaleix, A., Roussakis, E., Ducros, M., Houssen, Y.G., Vinogradov, S.A., Charpak, S., 2011. Nat. Med. 17 (7), 893–898.
Li, X., Zhao, X., Fang, Y., Jiang, X., Duong, T., Fan, C., Huang, C.C., Kain, S.R., 1998. J. Biol. Chem. 273 (52), 34970–34975.
Lidsky, P.V., Lukyanov, K.A., Misra, T., Handke, B., Mishin, A.S., Lehner, C.F., 2018. Development 145 (4), dev156257.
Maritan, S.M., Lian, E.Y., Mulligan, L.M., 2017. J. Vis. Exp. 121, 55544.
Merrill, A.H., Lambeth, J.D., Edmondson, D.E., Mccormick, D.B., 1981. Annu. Rev. Nutr. 1, 281–317.
Metzger, W., Sossong, D., Bächle, A., Pütz, N., Wennemuth, G., Pohlemann, T., Oberringer, M., 2011. Cytotherapy 13 (8), 1000–1012.
Misra, T., Baccino-Calace, M., Meyenhofer, F., Rodriguez-Crespo, D., Akarsu, H., Armenta-Calderón, R., Gorr, T.A., Frei, C., Cantera, R., Egger, B., Luschnig, S., 2017. Biol Open 6 (2), 296–304.
Mueller-Klieser, W., Freyer, J.P., Sutherland, R.M., 1986. Br. J. Cancer 53, 345–453.
Nagai, T., Yamada, S., Tominaga, T., Ichikawa, M., Miyawaki, A., 2004. Proc. Natl. Acad. Sci. USA 101, 10554–10559.
Nogales, D., Lightner, D.A., 1995. J. Biol. Chem. 270, 73–77.
Nunn, A., Linder, K., Strauss, H.W., 1995. Eur. J. Nucl. Med. 22, 265–280.
Ortiz-Prado, E., Dunn, J.F., Vasconez, J., Castillo, D., Viscor, G., 2019. Am. J. Blood. Res. 9 (1), 1–14.
Panicucci, G., Iacopino, S., De-Meo, E., Perata, P., Weits, D.A., 2020. Biosensors 10 (12), 197.
Papkovsky, D.B., Dmitriev, R.I., 2013. Chem. Soc. Rev. 42, 8700–8732.
Papkovsky, D.B., Dmitriev, R.I., 2018. Cell. Mol. Life Sci. 75, 2963–2980.
Peresse, T., Gautier, A., 2019. Int. J. Mol. Sci. 20 (24), 6142.
Peter, M., Ameer-Beg, S.M., Hughes, M.K.Y., Keppler, M.D., Prag, S., Marsh, M., Vojnovic, B., Ng, T., 2005. Biophys. J. 88 (2), 1224–1237.
Potzkei, J., Kunze, M., Drepper, T., Gensch, T., Jaeger, K.E., Büchs, J., 2012. BMC Biol. 10, 28.
Prost-Fingerle, K., Hoffmann, M.D., Schützhold, V., Cantore, M., Fandrey, J., 2017. Exp. Cell Res. 356, 122–127.
Raleigh, J.A., Dewhirst, M.W., Thrall, D.E., 1996. Semin. Radiat. Oncol. 6, 37–45.
Remington, S.J., 2006. Curr. Opin. Struct. Biol. 16, 714–721.
Rogers, S., Wells, R., Rechsteiner, M., 1986. Science 234, 364–368.
Roussakis, E., Li, Z., Nichols, A.J., Evans, C.L., 2015. Angew. Chem. Int. Ed. Engl. 54, 8340–8362.
Schindelin, J., Arganda-Carreras, I., Frise, E., Kaynig, V., Longair, M., Pietzsch, T., Preibisch, S., Rueden, C., Saalfeld, S., Schmid, B., Tinevez, J.-Y., White, D.J., Hartenstein, V., Eliceiri, K., Tomancak, P., Cardona, A., 2012. Nat. Methods 9, 676–682.
Schmitz, C., Pepelanova, I., Seliktar, D., Potekhina, E., Belousov, V.V., Scheper, T., Lavrentieva, A., 2020. Biotechnol. Bioeng. 117, 3265–3276.
Schmitz, C., Potekhina, E., Belousov, V.V., Lavrentieva, A., 2021. Front. Bioeng. Biotechnol. 9, 611837.
Shamirian, A., Afsari, H.S., Hassan, A., Miller, L.W., Snee, P.T., 2016. ACS Sens. 1 (10), 1244–1250.
Shaner, N.C., Lin, M.Z., Mckeown, M.R., Steinbach, P.A., Hazelwood, K.L., Davidson, M. W., Tsien, R.Y., 2008. Nat. Methods 5, 545–551.
Sillen, A., Engelborghs, Y., 1998. Photochem. Photobiol. 67 (5), 475–486.
Span, P.N., Bussink, J., 2015. Semin. Nucl. Med. 45 (2), 101–109.
Takahashi, E., Takano, T., Nomura, Y., Okano, S., Nakajima, O., Sato, M., 2006. Am. J. Physiol. Cell Physiol. 291 (4), C781–C787.
Thomlinson, R.H., Gray, L.H., 1955. Br. J. Cancer 9 (4), 539–549.
Wegmann, F., Petri, B.R., Khandoga, A.G., Moser, C., Khandoga, A., Volkery, S., Li, H., Nasdala, I., Brandau, O., FäSsler, R., Butz, S., Krombach, F., Vestweber, D., 2006. J. Exp. Med. 203 (7), 1671–1677.
Wu, B., Wu, Y., Tang, W., 2019. Front. Pharmacol. 10, 825.
Wu, C., Bull, B., Christensen, K., Mcneill, J., 2009. Angew. Chem. Int. Ed. Engl. 48 (15), 2451–2455.
Yoshihara, T., Yamaguchi, Y., Hosaka, M., Takeuchi, T., Tobita, S., 2012. Angew. Chem. Int. Ed. Engl. 1 (17), 4148–4151.
Youssef, S., Ren, W., Ai, H.-W., 2016. ACS Chem. Biol. 11, 2492–2498.